May 31st, 2:10 PM - 2:25 PM

Interfacial velocity estimation in highly aerated stepped spillway flows with a single tip fibre optical probe and Artificial Neural Networks

D. Valero
Aachen University of Applied Sciences, University of Liege

D. B. Bung
Aachen University of Applied Sciences

DOI:10.15142/T3Q590

Interfacial velocity estimation in highly aerated stepped spillway flows with a single tip fibre optical probe and Artificial Neural Networks

D. Valero[1, 2] and D. B. Bung[1]
[1]Hydraulic Engineering Section (HES)
FH Aachen University of Applied Sciences
Aachen, Germany
[2]Dept. of ArGEnCo, Research Group of Hydraulics in Environmental and Civil Engineering (HECE)
University of Liege (ULg)
Liège, Belgium
E-mail: valero@fh-aachen.de

ABSTRACT

Air-water flows can be found in different engineering applications: from nuclear engineering to huge hydraulic structures. In this paper, a single tip fibre optical probe has been used to record high frequency (over 1 MHz) phase functions at different locations of a stepped spillway. These phase functions have been related to the interfacial velocities by means of Artificial Neural Networks (ANN) and the measurements of a classical double tip conductivity probe. Special attention has been put to the input selection and the ANN dimensions. Finally, ANN have shown to be able to link the signal rising times and plateau shapes to the air-water interfacial velocity.

Keywords: *air-water flows, Artificial Neural Networks, air-water interfacial velocity, stepped spillways*

1. INTRODUCTION

Air-water flows can be easily found in large hydraulic structures, where self-aeration occurs as a complex and turbulent air-water compatibility phenomenon (Valero and Bung 2016). In spillway flows, researchers' efforts have focused both in the aerated regions (Zhang and Chanson 2016a, Bung 2011, Felder and Chanson 2011, Boes and Hager 2003, Chanson and Toombes, 2002) and non-aerated regions (Valero and Bung 2016, Zhang and Chanson 2016b, Meireles et al. 2014, Meireles et al. 2012, Amador et al. 2006); while some unresolved key challenges still exist (Matos and Meireles 2014, Chanson 2013). Hydraulic jumps have been also a common case of air-water flow studies as the impingement induced aeration plays a main role (Murzyn et al. 2005, Wang and Murzyn 2016, Wang and Chanson 2015, Wang et al. 2014, Chanson and Brattberg 2002).

Although some new non-intrusive techniques are available (Bung and Valero 2016, Bung and Valero 2015, Felder and Chanson 2014, Nóbrega et al. 2014, Leandro et al. 2014, Bung 2013, Chachereau and Chanson 2011, Kucukali and Chanson 2008, Misra et al. 2006), intrusive techniques have been more widely used (Wang et al. 2014, Boes and Hager 2003, Chanson and Brattberg 2002). When the air fraction C, or water fraction $(1 - C)$ exceeds 1 to 3 %, accuracy of common instrumentations for single phase flow measurements is typically affected and conductivity/optical probes become the best option (Felder and Chanson 2015). However, when using intrusive measurement techniques, some drawbacks and limitations can arise (Borges et al. 2010). In order to save some difficulties involved in air-water flow velocity measurements, Artificial Intelligence (AI) techniques have recently been used (Bung and Valero 2016a). Optical fibre probes work based upon the difference on light refraction at air/water interfaces. Usually, when velocity measurement is required, these probes comprise two conical tips. First and second tip are intended to record two signals based on the same bubbly events. Then, by cross-correlating the signals the most probable lag time can be obtained. Altogether with the known distance between both probes, a velocity may be computed. Nonetheless, a second option is available based on a single tip configuration.

In this study, raw signals are recorded in a highly aerated flow on a moderately sloped stepped spillway; similar to the setups described in Bung and Valero (2015) and Bung (2011). These signals, altogether with the previously obtained information, are later processed and used to train different Artificial Neural Networks (ANN) configurations by using PyBrain open-source package (Schaul et al. 2010).

2. EXPERIMENTAL SETUP

2.1. Stepped spillway

All measurements have been conducted in a moderately sloped stepped spillway (1V:2H, ϕ = 26.56º) with step height s = 6 cm for three different flow rates q = 0.07, 0.09 and 0.11 m^2/s. Total drop height is 1.74 m with a width of 0.50 m. Water was pumped from a lower basin into an open head tank from where it was conveyed into the stepped chute via an approaching channel of 1 m length. In order to complete a wider range of air concentrations, measurements have been conducted at steps (E) 13, 14, 18, 19 and 21; being the flow fully developed at step 21 for the highest discharge (see Fig. 1).

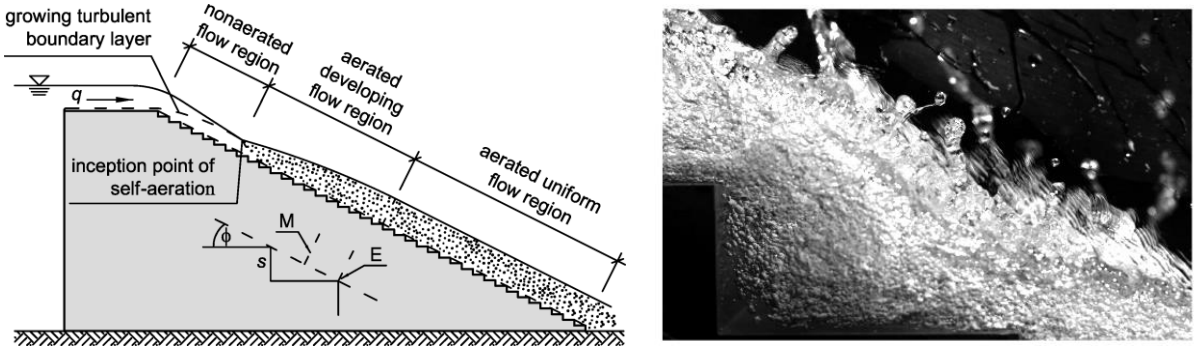

Figure 1. Sketch of flow regions over a spillway (left) and aerated flow at step 21 for q = 0.07 m^2/s (right).

2.2. Single tip optical probe description and settings

Since the early study of Neal and Bankoff (1963), phase detection probes have become a common measuring technique in multiphase flows disciplines. In this study, a single tip optical probe is employed (Fig. 2). This probe (also known as mono-optical probe) has been placed in the centreline of the spillway, over the step edges. As shown in Fig. 2, the probe is moved by a CNC controlling system (isel) with an accuracy of ~0.1 mm. The probe is manufactured and distributed by A2 Photonic Sensors, including a signal recording and analyser software and an optoelectronic module.

Vertical interfacial velocity profiles (raw signals) have been recorded perpendicularly to the pseudo-bottom with 2 mm spacing, at steps 13, 14, 18, 19 and 21, resulting in 646 measurements.

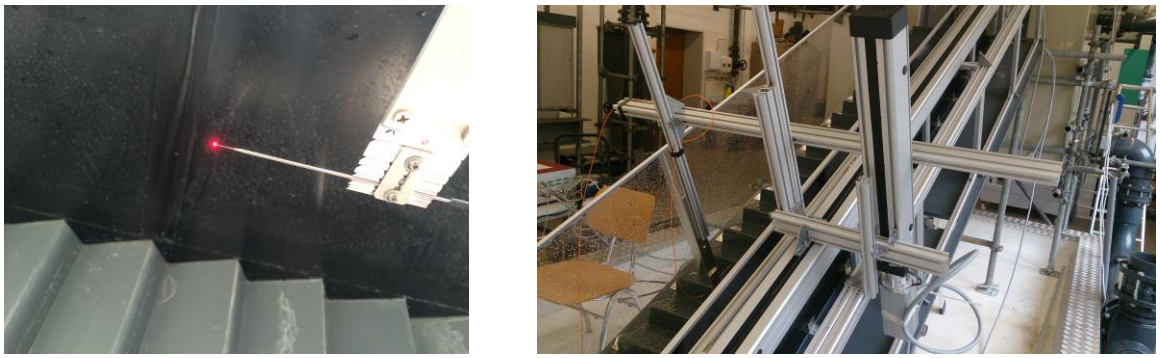

Figure 2. Monofibre optical probe location (left) and 2D controlling system configuration (right).

Single optical phase detection probes are able to measure gas velocities provided that their sensitive length (or latency length, L) is accurately known (Cartellier 1998, Cartellier and Barrau 1998a, b). To avoid a certain level of sensitivity to uncontrollable parameters (i.e.: angle of the impact on the bubble interface), probes geometry can differ from the commonly used dual tip optical fibres. Thus, more complex geometries can be used

(Cartellier and Barrau 1998b), e.g.: a cone + cylinder + cone geometry where the tip reduces its inner diameter through an intermediate cone. However, the employed probe corresponds to a simple cone geometry, which is more sensitive to uncontrolled parameters.

Air-water interface velocity can be approximated by using:

$$v = L \cdot {t_r}^b \tag{1}$$

where t_r is called the rising time, which represents the time it takes the signal to pass from level 10% to 90% of the air level, b is a dimensionless parameter taking a value close to –1 to correct the estimation and L depends on the probe's tip length. For the employed probe, b = –1.02 and L takes the value of 45.3 μm when the rising times are taken in microseconds to obtain the velocity in meters per second. Threshold levels 10% and 90% are based on the provider's experience and directly affect the values taking the other parameters.

Cartellier (1998) reports a relative error of around 10 % both for air fraction and gas flux, while the provider points out that an error of 15 % can be expected for the used probe. Further discussion on the probe/bubble interaction and the effect upon the air fraction measurement accuracy can be found in Vejražka et al. (2010). Errors are globally comparable for the monofibre and the bi-probe techniques, but these techniques are not equally sensitive to the flow regime. For finely dispersed flows, monofibre optical probes are better suited while double tip probes seem better adapted whenever large gas inclusions are present (Cartellier 1998). This makes a challenge for monofibre probes to measure in highly turbulent aerated spillway flows. Also, their actual response is sensitive to small geometrical defects occurring at their tips as pointed out by Cartellier and Barrau (1998a, b). This fact underlines the benefit of using more complex techniques than the rise time/velocity correlation provided by Eq. 1.

In order to obtain an accurate estimation of t_r, the sampling rate has been set to 1 MHz, being around 50 times larger than the minimum recommended sampling rate for dual tip probes for similar types of flows, where only small discrepancies can be observed in the turbulence estimations at a higher sampling frequency of 20 to 40 KHz (Felder and Chanson 2015). The sampling duration is recommended to be over 45 s, however in the study of Felder and Chanson (2015) only small differences can be observed over 20 s for similar flows. André et al. (2005) investigated the effects of sampling duration upon the interfacial velocity and the cross-correlation coefficient and suggested a sampling duration of more than 30 s. Consequently, the sampling duration has been set to 30 seconds, yielding over 30 million data points per recorded signal and nearly 20,000 million data points considering the entire set of recorded signals.

3. SIGNAL ANALYSIS

As described above, 646 million raw signals have been recorded, obtaining 30 million data points at each location to be later analyzed and used to train and test the artificial neural network employed in this study. Each signal displays a signature every time that a bubble impacts the monofibre probe tip (see Fig. 3 for an exemplary bubble event), which may provide a large amount of information.

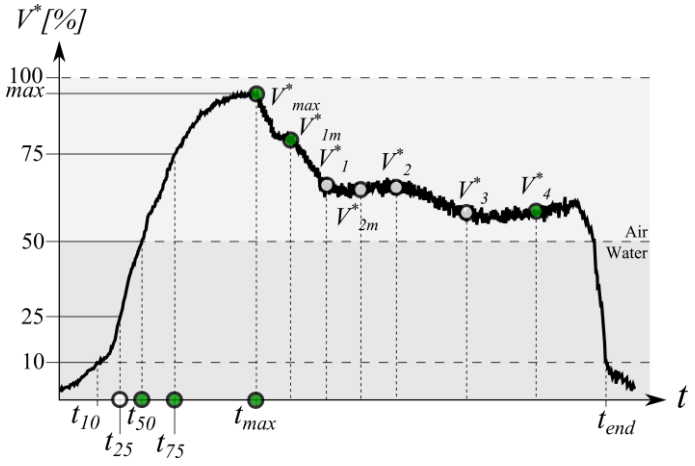

Figure 3. Exemplary signal of a bubble-tip impact extracted from the phase function recorded by the single tip probe, main features and ANN input definition (variables marked in green).

High frequency small amplitude oscillations can be observed in the data files which may affect the analysis of the phase indicator function. To remove these small oscillations, a central moving average filter with a moving window of 10 time steps (at a time resolution of 1 MHz produces a 1 μs signal delay) has been applied. By removing sampled frequencies above a certain cutoff frequency, the moving average creates a smoothing effect which has shown to remove effectively the noise. Further information on application of similar and more complex filtering techniques to air-water measurements can be found in the study of Bung and Valero (2015).

In order to make the signal independent from the used voltage range, water and air levels defined with the providers' software, all the signals have been scaled to be comprised between 0 and 100 %; thus a normalized voltage (V^*) results, but an air-water voltage range over 5 Volts was always ensured in the original recordings. Every recording included thousands of events (i.e. phase changes from water to air or bubble/droplet impacts). To make the ANN independent of the number of events and the bubble size, a median signature (or median phase indicator function) has been extracted from each recording. Different parameters defining this median phase indicator function have been selected, which may be separated in (a) rising time parameters and (b) phase indicator shape parameters. As defined in Fig. 3, rising time related variables are:

- t_{10-25}, which is the difference between the time the dimensionless voltage V^* reaches the 25 % value (t_{25}) and the time it reached the 10 % value (t_{10}).
- t_{25-50}, which is the difference between the time the dimensionless voltage V^* reaches the 50 % value (t_{50}) and the time it reached the 25 % value (t_{25}).
- t_{50-75}, which is the difference between the time the dimensionless voltage V^* reaches the 75 % value (t_{75}) and the time it reached the 50 % value (t_{50}).
- t_{75-max}, which is the difference between the time the dimensionless voltage V^* reaches the maximum value (V^*_{max}) at the time t_{max} and the time it reached the 75 % value (t_{75}).

The phase indicators shape variables (also defined in Fig. 3) are:

- V^*_{max} is the dimensionless maximum value reached by the signature at each event, close to 100 %.
- V^*_1, V^*_2, V^*_3 and V^*_4 split the signal from t_{max} to t_{end} (where the signal crosses the 10% value again) in five equal portions.
- V^*_{1m} and V^*_{2m} are the normalized voltages measurements between V^*_{max} and V^*_1, V^*_1 and V^*_2 respectively. These extra voltages where selected to better describe the exponentially decreasing tail which can be usually observed after the V^*_{max} takes place.

All these time and phase parameters have been chosen arbitrarily based on a better representation of the overall phase function.

4. ARTIFICIAL NEURAL NETWORK FOR INTERFACIAL VELOCITY ESTIMATION

4.1. Introduction

Artificial Neural Networks (ANN), one of the earliest techniques of Artificial Intelligence, have become a powerful tool for prediction and forecasting of water resources, being a large number of studies published recently addressing mainly hydrological (Maier et al. 2010) and sediment problems. However, when it comes to hydraulic instrumentation prediction improvement, only a few attempts are documented. Carosone et al. (1995) and Chen et al. (1998) employed neural networks altogether with Particle Tracking Velocimetry (PTV) and Particle Image Velocimetry (PIV) techniques. Recently, Bung and Valero (2016a) and Bung and Valero (2016b) have applied Artificial Intelligence techniques obtaining, at least, as accurate velocity fields as classical cross-correlation based techniques for bubbly and swirling flows.

All ANN models take the form:

$$Y = f(X, W) + \varepsilon \tag{2}$$

Where Y is the vector of model outputs, X is the vector of model input, W the vector of model parameters (or connection weights), $f(\cdot)$ is a functional relationship between model outputs, inputs and parameters; and ε is the

vector of model errors. The functional relationship depends strongly on the ANN architecture (e.g.: the number of hidden layers and number of neurons). In this study, the model output is a single scalar (velocity, v), the vector of model input is discussed in Section 4.2 on the basis of the event-driven description of the recorded signal; the number of neurons is discussed in Section 4.3 and the vector of model errors is the result of the ANN training, discussed in Section 4.4. All the described operations have been carried out by using Python 2.7, altogether with PyBrain 0.3 for the ANN setup (Schaul et al. 2010) and Matplotlib 1.5 (Hunter 2007) for scientific plotting.

4.2. Input selection

One of the most important steps in the ANN model development process is the determination of an appropriate set of inputs (X). However, this task is generally given little attention in ANN modelling and most inputs are determined on an ad-hoc basis or using a priori system knowledge (Maier et al. 2010).

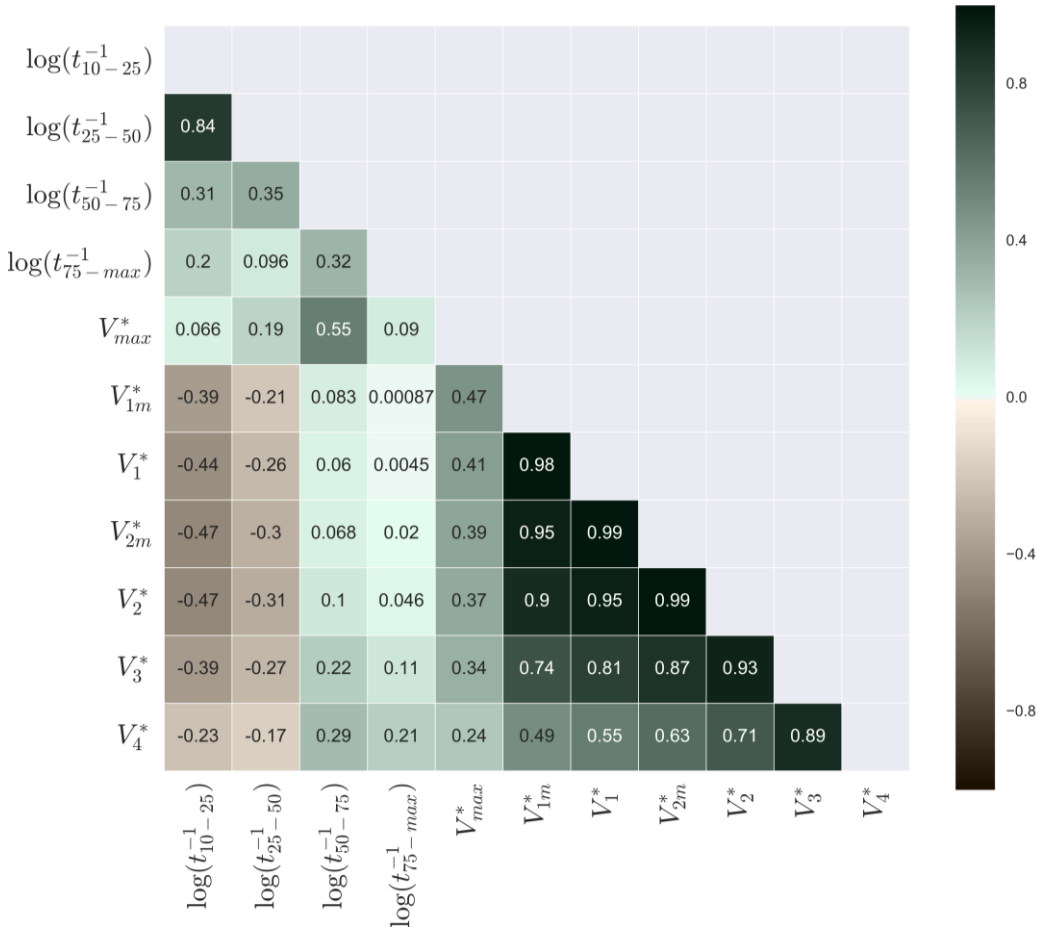

Figure 4. Correlation matrix for the signal descriptors marked in Fig. 3.

All the variables marked in Fig. 3 are obtained for each event of the 646 measurements. This yields thousands of values for each measurement. In order to get only one value per signal, the median value is computed. Temporal variables are inverted (t^{-1}) which physically represents a velocity – instead of a time – and the shape parameters are selected based on the observed fact that the bubble impacting the tip produces a characteristic signature (Cartellier 1998, Cartellier and Barrau 1998a, b). In order to make the shape parameters independent from the event duration (and consequently from the bubble size), they have been selected by splitting the plateau of each event in equal parts. For the temporal variables, a logarithmic distribution has been noticed. Consequently, logarithm of t^{-1} is used to obtain a more homogeneous distribution.

Given a fixed number of training samples, the addition of redundant model inputs increases the ratio of the number of connection weights to the number of training samples, thus increasing the likelihood of overfitting, while not providing any additional information to the model. Secondly, the inclusion of redundant model inputs introduces additional local minima in the error surface in weight space (Maier et al. 2010). To detect redundancy between the described variables, correlation among them has been computed (see Fig. 4).

A strong correlation between the shape variables has been observed in the tail of the signal while V^*_{max}, V^*_{1m} and V^*_4 were less correlated. Thus, the other shape variables have been disregarded. Within the temporal variables, only t_{10-25} were found to be correlated to t_{25-50}. Given that t_{10-25} is more correlated to the remaining parameters than t_{25-50}, the former one has been neglected. Consequently, selected variables for the ANN input vector (marked in green in the Fig. 3) are the following:

$$X = [\log({t_{25-50}}^{-1}), \log({t_{50-75}}^{-1}), \log({t_{75-max}}^{-1}), {V^*}_{max}, {V^*}_{1m}, {V^*}_4] \quad (3)$$

Every element of the vector of model inputs is normalized between −1 and 1; which makes the training faster.

4.3. ANN architecture

The ANN of this study is a feedforward network with six input neurons and one output neuron and full connectivity (see Fig. 5). The dimensions of the input and output layers are directly determined by the selected inputs (Eq. 3) and the choice of the desired output or target (herein the interfacial velocity). However, dimensions of the hidden layer and the number of layers have undergone an iterative process. While one hidden layer can identify simple patterns, two can guarantee recognition of more complex patterns. Usually, it is not recommended to go over three hidden layers. In this study, two hidden layers have been selected. Different types of transfer functions between neurons have been examined, obtaining the best results for linear (input layer), sigmoid (hidden layer 1 and 2) and linear (output layer). Other types of transfer functions are available in PyBrain (Schaul et al. 2010) and in the literature (Rojas 2013).

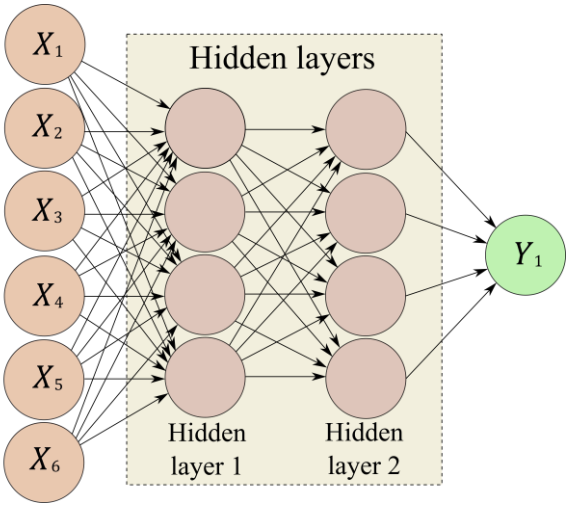

Figure 5. ANN architecture: feedforward network with full connectivity, 6 input neurons, 2 hidden layers and 1 output layer.

4.4. ANN training and testing

As ANNs are prone to overfitting the calibration data, cross-validation is generally used, as part of which the calibration data are divided into training and testing subsets (Maier et al. 2010). The available dataset (646 samples) has been divided in training and testing subsets with a proportion of 70 % and 30 % respectively (452 and 194 samples respectively). The training algorithm adjusts the parameters reducing the mean squared error (MSE, as defined by Bennett et al. 2013) for the training subset while tracking the effect upon the testing subset. When the error in the testing subset stops decreasing the training is stopped (see Fig. 6). The iterations are commonly called epochs.

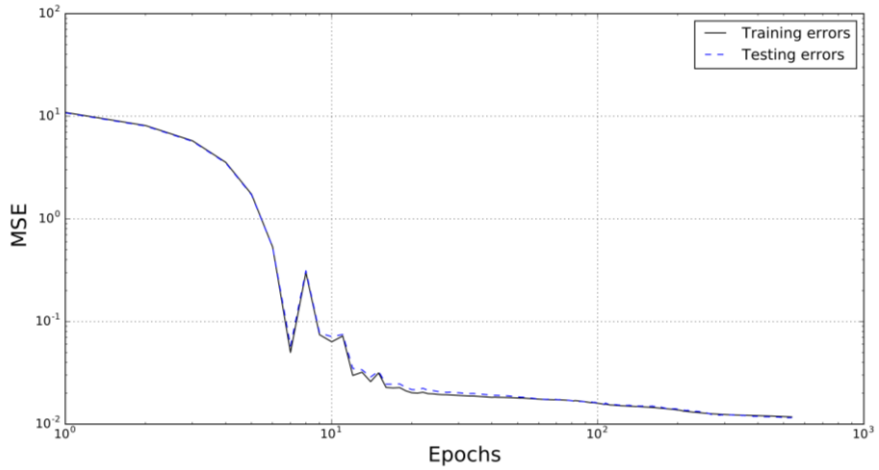

Figure 6. Training with cross validation for the ANN model. Mean squared error (MSE, as defined by Bennett et al. 2013).

The employed training algorithm is RProp- of Igel and Hüsken (2003) with all training samples with the same weight. Classic backpropagation algorithm has been also used resulting usually in a worst training.

5. RESULTS

Alternatively to the MSRE computed in the training process, the correlation coefficient (r) as defined by Bennet et al. (2013) has been computed to assess both Eq. 1 and ANN performance; which is commonly used for model evaluation. In Fig. 7, r values are shown for ANN training and testing datasets for a total number of 2541 trainings (21 per combination). It is clearly observed that all shown combinations provide a r value over 70 % for both training and testing datasets for all of the studied number of neurons in the hidden layers; and a maximum value of 88.9 % and 81.9 % respectively.

In Fig. 7 it can be also observed that higher number of neurons in the hidden layers improves the accuracy for the training datasets while it suddenly stabilizes for the testing dataset. As the number of samples does not increase, a smaller number of neurons for the same accuracy level might be desirable. Consequently, a combination of five neurons in the hidden layer one with five neurons in the hidden layer two has been selected to show the ANN results (see Fig. 8). In order to illustrate utility of the present ANN, results from Eq. 1 are also shown in Fig. 8.

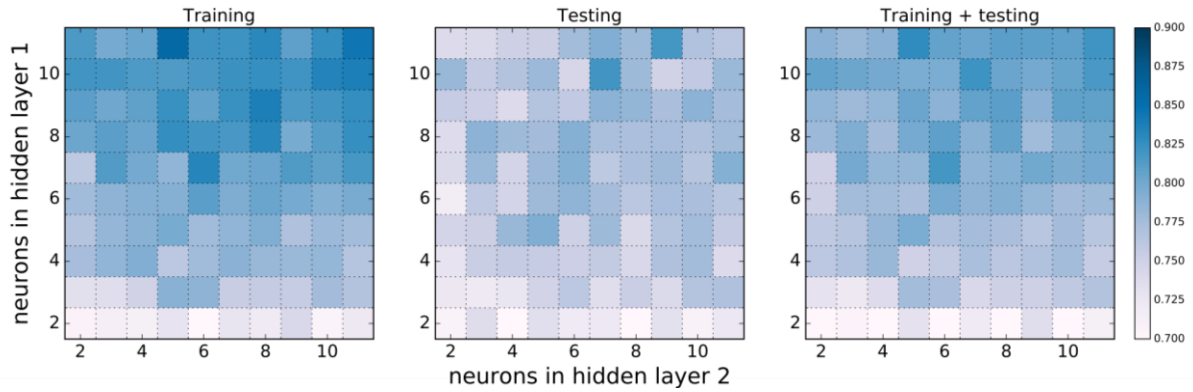

Figure 7. Best correlation coefficient for training (left), testing (center) and all dataset (right) after 21 trainings until convergence and different neurons number in the hidden layers.

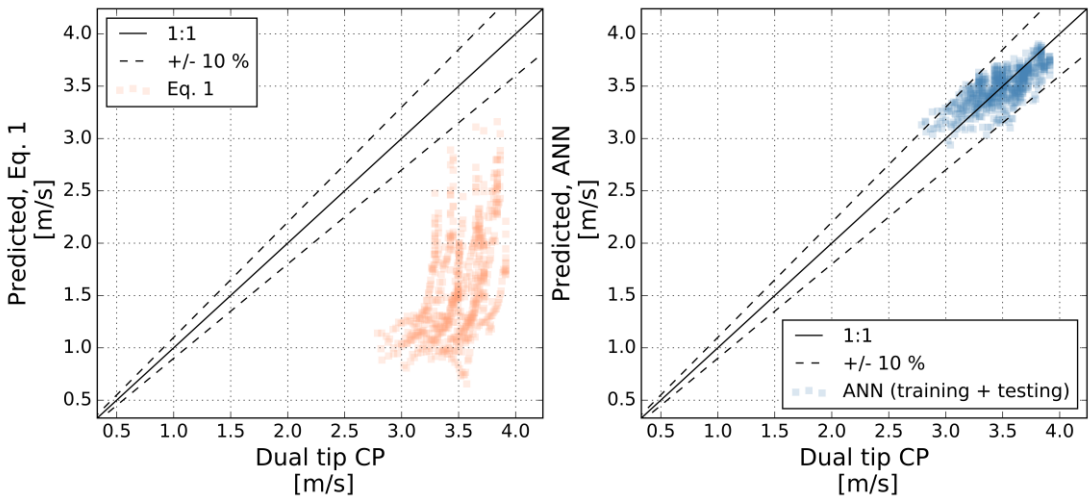

Figure 8. Dual tip conductivity probe (CP) measurements of Bung (2011) and predicted interfacial velocity of the quasilinear Eq. 1 (left) and the ANN (right).

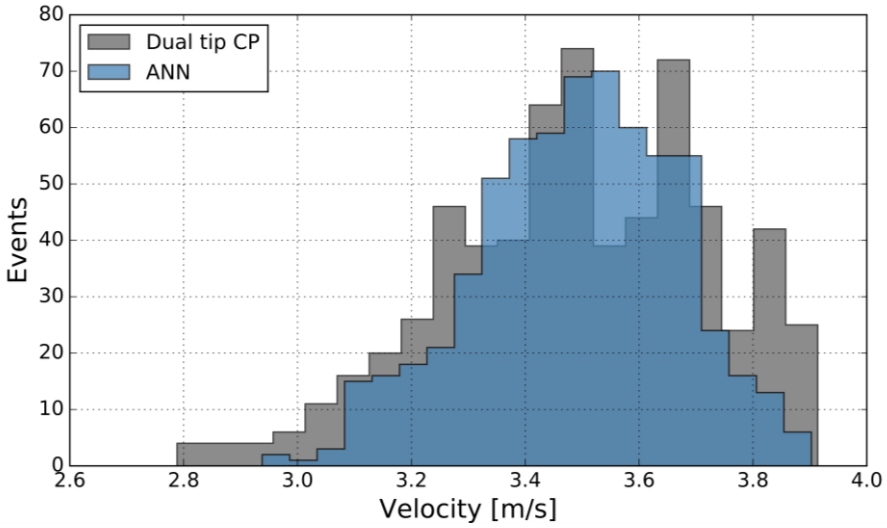

Figure 9. Interfacial velocities histograms for the cross-correlation based velocity of Bung (2011) and the ANN approach presented herein.

6. CONCLUSIONS

In this study, a large number of measurements with a single tip optical fibre probe have been performed in a 1V:2H stepped spillway. Measurements have been conducted every 2 mm at different steps, obtaining different velocities at regions of different aeration. After a correlation analysis (see Fig. 4), some irrelevant parameters have been discarded, finally selecting three temporal parameters and three phase function shape parameters as input for a feedforward ANN. Choice of these initially proposed parameters is based on previous studies observations, which showed that rising times are related to the interfacial velocities and that signature shape may depend on small geometrical defects occurring at the probes tips (Cartellier and Barrau 1998a, b).

When using an ANN approach, non-linear model flexibility allows reproducing complex patterns and detection of important relations which could remain unseen otherwise. The proposed ANN counts on two hidden layers and one output (the interfacial velocity). The number of neurons in the hidden layers has been the result of an iterative process, as shown in Fig. 7, where training performance has been studied accounting also for the dimension of the network thus avoiding over fitting.

In this study, improvement of the predictions has shown to be significant when compared to the initial proposed model. Accuracy enhancement of ANN model over the quasilinear approach (Eq. 1) can be observed in Figs. 8 and 9. Majority of ANN predictions fall within the +/− 10 error, showing higher difficulty to reproduce extreme values.

7. ACKNOWLEDGMENTS

Authors thank A2 Photonic Sensors for providing the instrumentation, installation recommendations and for their kind attention.

8. REFERENCES

Amador, A., Sánchez-Juny, M., and Dolz, J. (2006). Characterization of the non-aerated flow region in a stepped spillway by PIV. *Journal of Fluids Engineering*, 128(6), 1266–1273. doi:10.1115/1.2354529

André, S., Boillant, J.L., Schleiss, J.L. (2005). Two-Phase Flow Characteristics of Stepped Spillways. Discussion, Journal of Hydraulic Engineering, 131(5), 423-427. doi: 10.1061/(ASCE)0733-9429(2005)131:5(423)

Bennett, N. D., Croke, B. F., Guariso, G., Guillaume, J. H., Hamilton, S. H., Jakeman, A. J., Marsili-Libelli, S., Newham, L. T., Norton, J. P., Perrin, C. and Pierce, S. A. (2013). Characterising performance of environmental models. *Environmental Modelling & Software*, 40, 1-20. doi:10.1016/j.envsoft.2012.09.011

Boes, R., and Hager, W. H. (2003). Two-Phase Flow Characteristics of Stepped Spillways. *Journal of Hydraulic Engineering*, 129(9), 661-670. doi: 10.1061/(ASCE)0733-9429(2003)129:9(661)

Borges, J. E., Pereira, N. H., Matos, J., and Frizell, K. H. (2010). Performance of a combined three-hole conductivity probe for void fraction and velocity measurement in air–water flows. *Experiments in fluids*, 48(1), 17-31. doi: 10.1007/s00348-009-0699-1

Bung, D. B. (2011). Developing flow in skimming flow regime on embankment stepped spillways. *Journal of Hydraulic Research*, 49(5), 639-648. doi: 10.1080/00221686.2011.584372

Bung, D. B. (2013). Non-intrusive detection of air–water surface roughness in self-aerated chute flows. *Journal of Hydraulic Research*, 51(3), 322-329. doi: 10.1080/00221686.2013.777373

Bung, D. B., and Valero, D. (2015). Image Processing for Bubble Image Velocimetry in Self-aerated Flows. *E-proceedings of the 36th IAHR World Congress*, 28 June – 3 July, 2015, The Hague, the Netherlands. ISBN: 978-90-824846-0-1

Bung, D. B., and Valero, D. (2016a). Optical flow estimation in aerated flows. *Journal of Hydraulic Research*, 1-6. doi: 10.1080/00221686.2016.1173600

Bung, D. B., and Valero, D. (2016b). Application of the Optical Flow Method to Velocity Determination in Hydraulic Structure Models. Proc., *6th International Symposium on Hydraulic Structures*, Portland, Oregon, USA, 27-30 June 2016.

Carosone, F., Cenedese, A., and Querzoli, G. (1995). Recognition of partially overlapped particle images using the Kohonen neural network. *Experiments in Fluids*, 19(4), 225-232. doi: 10.1007/BF00196470

Cartellier, A. (1998). Measurement of gas phase characteristics using new monofiber optical probes and real-time signal processing. *Nuclear Engineering and Design*, 184(2-3), 393-408. doi: 10.1016/S0029-5493(98)00211-8

Cartellier, A., and Barrau, E. (1998a). Monofiber optical probes for gas detection and gas velocity measurements: conical probes. *International Journal of Multiphase Flow*, 24(8), 1265-1294. doi: 10.1016/S0301-9322(98)00032-9

Cartellier, A., and Barrau, E. (1998b). Monofiber optical probes for gas detection and gas velocity measurements: optimized sensing tips. *International Journal of Multiphase Flow*, 24(8), 1295-1315. doi: 10.1016/S0301-9322(98)00033-0

Chachereau, Y., and Chanson, H. (2011). Free-surface fluctuations and turbulence in hydraulic jumps. *Experimental Thermal and Fluid Science*, 35(6), 896-909. doi: 10.1016/j.expthermflusci.2011.01.009

Chanson, H., and Brattberg, T. (2002). Experimental study of the air–water shear flow in a hydraulic jump. *International Journal of Multiphase Flow*, 26(4), 583-607. doi:10.1016/S0301-9322(99)00016-6

Chanson, H. and Toombes, L. (2002). Air–water flows down stepped chutes: turbulence and flow structure observations. International Journal of Multiphase Flow, 28(11), 1737-1761. doi: 10.1016/S0301-9322(02)00089-7

Chanson, H. (2013). Hydraulics of aerated flows: qui pro quo?. *Journal of Hydraulic Research*, 51(3), 223-243.

Felder, S., and Chanson, H. (2011). Air–water flow properties in step cavity down a stepped chute. *International Journal of Multiphase Flow*, 37(7), 732-745. doi: 10.1016/j.ijmultiphaseflow.2011.02.009

Chen, P. –H., Yen, J. –Y., and Chen, J. –L. (1998). An artificial neural network for double exposure PIV image analysis. *Experiments in Fluids*, 24(5), 373-374. doi: 10.1007/s003480050185

Felder, S., and Chanson, H. (2014). Air–water flows and free-surface profiles on a non-uniform stepped chute. *Journal of Hydraulic Research*, 52(2), 253-263. doi: 10.1080/00221686.2013.841780

Felder, S., and Chanson, H. (2015). Phase-detection probe measurements in high-velocity free-surface flows including a discussion of key sampling parameters. *Experimental Thermal and Fluid Science*, 61, 66-78. doi: 10.1016/j.expthermflusci.2014.10.009

Hunter, J.D., 2007. Matplotlib: a 2D graphics environment. *Computing in Science & Engineering*, 9(3), 90-95. doi: 10.1109/MCSE.2007.55

Igel, C., and Hüsken, M. (2003). Empirical evaluation of the improved Rprop learning algorithms. *Neurocomputing*, 50, 105-123. doi: 10.1016/S0925-2312(01)00700-7

Kucukali, S., and Chanson, H. (2008). Turbulence measurements in the bubbly flow region of hydraulic jumps. *Experimental Thermal and Fluid Science*, 33(1), 41-53. doi: 10.1016/j.expthermflusci.2008.06.012

Leandro, J., Bung, D. B., Carvalho, R. (2014). Measuring void fraction and velocity fields of a stepped spillway for skimming flow using non-intrusive methods. *Experiments in Fluids*, 55:1732. doi: 10.1007/s00348-014-1732-6

Maier, H. R., Jain, A., Dandy, G. C., and Sudheer, K. P. (2010). Methods used for the development of neural networks for the prediction of water resource variables in river systems: Current status and future directions. *Environmental Modelling & Software*, 25(8), 891-909. doi:10.1016/j.envsoft.2010.02.003

Matos, J., and Meireles, I. C. (2014). Hydraulics of stepped weirs and dam spillways: Engineering challenges, labyrinths of research. *Proc., 5th International Symposium on Hydraulic Structures: Hydraulic Structures and Society-Engineering Challenges and Extremes*, Brisbane, Australia, 25-27 June 2014.

Meireles, I. C., Renna, F., Matos, J, and Bombardelli, F. A. (2012). Skimming, nonaerated flow on stepped spillways over roller compacted concrete dams. *Journal of Hydraulic Engineering*, 138(10), 870–877.

Meireles, I. C., Bombardelli, F. A., and Matos, J. (2014). Air entrainment onset in skimming flows on steep stepped spillways: an analysis. *Journal of Hydraulic Research*, 52(3), 375-385. doi: 10.1080/00221686.2013.87840

Misra, S. K., Thomas, M., Kambhamettu, C., Kirby, J. T., Veron, F., and Brocchini, M. (2006). Estimation of complex air–water interfaces from particle image velocimetry images. *Experiments in Fluids*, 40(5), 764-775. doi: 10.1007/s00348-006-0113-1

Murzyn, F., Mouaze, D., and Chaplin, J. R. (2005). Optical fibre probe measurements of bubbly flow in hydraulic jumps. International Journal of Multiphase Flow, 31(1), 141-154. doi: 10.1016/j.ijmultiphaseflow.2004.09.004

Neal, L. G., and Bankoff, L. G. (1963). A high resolution resistivity probe for determination of local void properties in gas-liquid flow. *AIChE Journal*, 9(4), 490-494. doi: 10.1002/aic.690090415

Nóbrega, J. D., Schulz, H. E., and Zhu, D. Z. (2014). Free surface detection in hydraulic jumps through image analysis and ultrasonic sensor measurements. *E-proccedings of the 5th IAHR International Symposium on Hydraulic Structures* (pp. 1-8). The University of Queensland. doi: 10.14264/uql.2014.42

Rojas, R. (1996). Neural networks: a systematic introduction. *Springer Science & Business Media.* doi: 10.1007/978-3-642-61068-4

Schaul, T., Bayer, J., Wierstra, D., Sun, Y., Felder, M., Sehnke, F., Rückstieß, T., and Schmidhuber, J. (2010). PyBrain. *The Journal of Machine Learning Research*, 11, 743-746.

Valero, D., and Bung, D. B. (2016). Development of the interfacial air layer in the non-aerated region of high-velocity spillway flows. Instabilities growth, entrapped air and influence on the self-aeration onset. *International Journal of Multiphase Flow*, 84, 66-74. doi:10.1016/j.ijmultiphaseflow.2016.04.012

Vejražka, J., Večeř, M., Orvalho, S., Sechet, P., Ruzicka, M. C., and Cartellier, A. (2010). Measurement accuracy of a mono-fiber optical probe in a bubbly flow. *International Journal of Multiphase Flow*, 36(7), 533-548. doi: 10.1016/j.ijmultiphaseflow.2010.03.007

Wang, H., Felder, S., and Chanson, H. (2014). An experimental study of turbulent two-phase flow in hydraulic jumps and application of a triple decomposition technique. *Environmental Fluid Mechanics*, 55:1775. doi: 10.1007/s00348-014-1775-8

Wang, H., and Chanson, H. (2015). Air entrainment and turbulent fluctuations in hydraulic jumps. Urban Water Journal, 12(6), 502-518. doi: 10.1080/1573062X.2013.847464

Wang, H., and Chanson, H. (2016). Experimental assessment of characteristic turbulent scales in two-phase flow of hydraulic jump: from bottom to free surface. *Environmental Fluid Mechanics*, 1-19. doi: 10.1007/s10652-016-9451-6

Zhang, G., and Chanson, H. (2016a). Interaction between free-surface aeration and total pressure on a stepped chute. *Experimental Thermal and Fluid Science*, 74, 368-381. doi:10.1016/j.expthermflusci.2015.12.011

Zhang, G., and Chanson, H. (2016b). Hydraulics of the Developing Flow Region of Stepped Spillways. I: Physical Modeling and Boundary Layer Development. *Journal of Hydraulic Engineering*, 04016015. doi: 10.1061/(ASCE)HY.1943-7900.0001138